# A 2D/3D Discrete Duality Finite Volume Scheme. Application to ECG simulation

Y. Coudière*
* *Université de Nantes, Laboratoire de Mathématiques Jean Leray, 2, rue de la Houssinière, 44322 Nantes Cedex, France*
Yves.Coudiere@univ-nantes.fr

C. Pierre†
† *Laboratoire de Mathématiques et de leurs Applications, CNRS, Université de Pau. av. de l'Université, BP 1155, 64013 Pau Cedex - France*
Charles.Pierre@univ-pau.fr

O. Rousseau‡
‡ *Department of Mathematics and Statistics, University of Ottawa, 585 King Edward Av., Ottawa (Ont), Canada K1N 6N5*
orous097@mathstat.uottawa.ca

R. Turpault*
* *Université de Nantes, Laboratoire de Mathématiques Jean Leray, 2, rue de la Houssinière, 44322 Nantes Cedex, France*
Rodolphe.Turpault@univ-nantes.fr

**Abstract**

This paper presents a 2D/3D discrete duality finite volume method for solving heterogeneous and anisotropic elliptic equations on very general unstructured meshes. The scheme is based on the definition of discrete divergence and gradient operators that fulfill a duality property mimicking the Green formula. As a consequence, the discrete problem is proved to be well-posed, symmetric and positive-definite. Standard numerical tests are performed in 2D and 3D and the results are discussed and compared with P1 finite elements ones. At last, the method is used for the resolution of a problem arising in biomathematics: the electrocardiogram simulation on a 2D mesh obtained from segmented medical images.

**Key words** : Finite volumes, Anisotropic heterogeneous diffusion, electrocardiology, 3D discrete duality method

# 1 Introduction

Computer models of the electrical activity in the myocardium are increasingly popular: the heart's activity generates an extracardiac electrical field in the torso, the measurement of which on the body surface is the well-known electrocardiogram (ECG). It gives a non-invasive representation of the cardiac electrical function. Understanding the various patterns of the ECG is a major challenge for scientists, with a great impact on potential clinical applications. The most up-to-date system of equations that models the (nonstationary) cardiac electrical field is called the *bidomain model*. It consists in complex reaction-diffusion equations that are coupled to a quasistatic electrical equilibrium equation for the extracardiac potential field. The simpler *modified* bidomain model is introduced in section 5.2. One of the equations of this model states that the extracardiac field, denoted by $\varphi$, is (for any $t > 0$) the solution of an anisotropic and heterogeneous elliptic equation of the form

$$-\operatorname{div}(G\nabla\varphi) = f \quad \text{in } \Omega, \tag{1}$$

$$\varphi = g \quad \text{on } \partial\Omega_D, \tag{2}$$

$$G\nabla\varphi \cdot \mathbf{n} = h \quad \text{on } \partial\Omega_N. \tag{3}$$

In our framework, $\Omega$ is a bounded domain of $\mathbb{R}^d$ ($d = 2, 3$) representing the whole torso, the vector $\mathbf{n}$ denotes the outward unit normal on the boundary $\partial\Omega$ and $\partial\Omega = \partial\Omega_D \cup \partial\Omega_N$. The functions $g$ and $h$ are Dirichlet and Neumann boundary data.

Furthermore, the domain $\Omega$ is split into several parts: $H$ for the heart and $\Omega_{\text{cavities}}$, $\Omega_{\text{lung}}$, $\Omega_0$ respectively for the ventricular cavities, the lungs and the remainder of the torso. The diffusion tensor $G = G(x)$ is symmetric, anisotropic in the heart $H$ and piecewise constant (discontinuous) in $\Omega \backslash H$, as described in eq. (27). Its coefficients are measurable functions on $\Omega$ such that:

$$\exists m > 0,\ \forall \xi \in \mathbb{R}^d, \quad m|\xi|^2 \leq \xi^T G(x)\xi \leq M|\xi|^2 \quad (\text{a.e. } x \in \Omega).$$

The weak solution to (1)-(3) is well-defined in $H^1(\Omega)$.

The meshes are built by processing some medical data. They are unstructured and reflect the heterogeneity of the media (figure 8).

We point out that flux continuity (conservativity) seems to be of major importance to compute ECGs. Finite volume methods are quite suited for such problems: they handle very well the media heterogeneity, the unstructured meshes and the conservativity constraint. Moreover, sharp reaction terms might induce numerical instabilities. In the case of simplified models in electrocardiology, finite volume methods have been shown in [10] to be well adapted to handle such instability problems.

Therefore, based on the 2D method as defined in [13, 17], this paper introduces a new 3D finite volume discretization for general linear elliptic equations on general meshes. Classically, the unknown is a function piecewise constant on the control volumes of a given primary mesh. One idea to compute the fluxes of diffusion on the interfaces between the control volumes is to use the formula of the *diamond scheme* [11, 8]: this method however necessitates to reconstruct vertex values which breaks

symmetry properties. The innovative idea proposed in [13, 17] is to consider these vertex values as numerical unknowns. In 2D, the resulting scheme combines two distinct finite volume schemes on two overlapping meshes, the primary mesh and a secondary mesh of control volumes built around the vertices. It has one unknown per cell and one unknown per vertex. This method can be formulated by introducing some discrete divergence and gradient operators. The framework is comparable to that of the mimetic method [4] because the operators satisfy a discrete duality relationship that mimics the Green formula, thus motivating the name *Discrete Duality Finite Volume* (DDFV). The analogy with the mimetic finite volume does not extend further, because the DDFV uses a specific 2-meshes formulation that yields an explicit and very simple expression of the gradients and fluxes.

The DDFV method has been successfully applied in 2D to the Laplace equation [13] and generalized to nonlinear equations [3] and to a div-curl problem in [12]. It was shown to provide accurate discretizations of the gradient in [16].

To our knowledge, very few attempts in generalizing the approach to 3D problems with heterogeneity and anisotropy have been made, because the functional duality property does not extend in a straightforward way. The 2D construction of the discrete duality relies on the fact that an interface between two neighboring primary mesh cells can also be seen as an interface between two neighboring secondary mesh cells, so that two partial derivatives are evaluated naturally using the two corresponding finite differences. In the 3D case, the gradient is evaluated using the finite differences between two neighboring primary cells and several finite differences in the interface. The interface has at least three vertices. Thus it cannot be related to a single interface of the secondary mesh, like in the 2D case. As a consequence, both the construction of the fluxes and of the duality relationship are not straightforward. A complex 3D DDFV scheme was proposed and tested in [18]. Two more 3D DDFV schemes have been very recently proposed in [2, 9].

A new simple 3D DDFV setting is proposed in this paper, that was developed in [21]. It is a 2-meshes method and the gradient and fluxes are still computed on the natural *diamond cells*, built around the faces of the primary mesh. The assumptions on the meshes and the spaces of discrete data are presented in section 2. The main point is that the discrete duality property between the discrete gradient and divergence operators is easily recovered. The discrete operators and the proof of the duality property are explained in section 3. As a consequence, the discrete problem is proved to be well-posed. The numerical convergence of the solution and the cost of the method are studied and compared in a simple situation to the convergence and cost of the standard $P^1$ finite element approximation. The scheme and the numerical tests are described and discussed in section 4. Finally the scheme is applied to a real-life application in electrocardiology. Section 5 is devoted to this application. It explains how the mesh has been generated from medical images, specifies the underlying mathematical model and shows ECGs computed with the DDFV method.

# 2 Meshes and Discrete Data

## 2.1 Meshes

Considering a polyhedral/polygonal open bounded domain $\Omega \subset \mathbb{R}^d$, $d = 2$ or $d = 3$, a mesh of $\Omega$ is defined as usual within the field of finite volume methods [15] as the data of the three following sets $\mathcal{M}$, $\mathcal{F}$ and $\mathcal{X}$. The elements of $\mathcal{M}$ are polyhedra $K, L$ in $\mathbb{R}^d$. The elements of $\mathcal{F}$ are polygons $\sigma$ subsets of affine hyperplanes of $\mathbb{R}^d$. The elements of $\mathcal{X}$ are points in $\mathbb{R}^d$ denoted by their coordinates $x_A$. These three sets being moreover asked to fulfill the following properties:

1. The set $\mathcal{M}$ is a nonoverlapping partition of $\Omega$ in the sense that $\cup_{K\in\mathcal{M}}\overline{K} = \overline{\Omega}$ and for all $K, L \in \mathcal{M}$, $K \neq L \Rightarrow K \cap L = \emptyset$. $\mathcal{M}$ is refered to as the primary mesh and control volumes $K \in \mathcal{M}$ as primary cells.

2. The set $\mathcal{F}$ is made of polygons in dimension $d-1$, it gathers exactly

   (2a) the interfaces $\sigma = K|L$, $K, L \in \mathcal{M}$, defined as $K|L = \overline{K} \cap \overline{L}$ whenever this intersection has a non zero $d-1$ dimensional measure.

   (2b) the remaining facets $\sigma = \partial\Omega \cap \partial K$ of the $K \in \mathcal{M}$;

3. The set $\mathcal{X}$ gathers the vertices $x_A$ of the facets $\sigma \in \mathcal{F}$.

The subset of $\mathcal{F}$ given by (2a) is the set of interfaces, denoted by $\mathcal{F}^i$ while its complementary given by (2b) is the set of boundary faces, denoted by $\mathcal{F}^b$. Similarly the subsets of $\mathcal{X}$ of the interior and boundary vertices are denoted by $\mathcal{X}^i$ and $\mathcal{X}^b$.

For any $K \in \mathcal{M}$, there exists a subset $\mathcal{F}_K$ of $\mathcal{F}$ such that $\partial K = \cup_{\mathcal{F}_K}\sigma$.

For the mesh to be adapted to the prescribed boundary conditions (2)-(3), the set $\mathcal{F}^b$ of boundary facets is split into two complementary subsets, $\mathcal{F}^b = \mathcal{F}^b_N \cup \mathcal{F}^b_D$ and $\mathcal{F}^b_D \cap \mathcal{F}^b_N = \emptyset$, in such a way that $\overline{\partial\Omega}_N = \cup_{\sigma\in\mathcal{F}^b_N}\sigma$ and $\overline{\partial\Omega}_D = \cup_{\sigma\in\mathcal{F}^b_D}\sigma$. One also denotes by $\mathcal{X}^b_D \subset \mathcal{X}^b$ the set of the vertices of all faces $\sigma \in \mathcal{F}^b_D$.

Every facet $\sigma \in \mathcal{F}$ as well as every primary cell $K \in \mathcal{M}$ is supplied with a center $x_\sigma \in \sigma$ and $x_K \in K$: in practice its isobarycenter.

Moreover, and this is noticeable, each facet $\sigma \in \mathcal{F}$ is required to be either a triangle or a quadrangle, more general faces leading to technical difficulties in the study of the discrete gradient, see remark 6. That general definition allows general meshes, in particular non-conformal ones. In this last case, the geometrical face of a cell is obtained by gathering two or more mesh interfaces, and some point $x_A \in \mathcal{X}$ are "hanging nodes" (see fig. 1).

The definition of the DDFV scheme requires the construction of two additional sets of control volume or meshes:

- the secondary - vertex based - mesh, denoted by $\mathcal{V}$, whose elements will be refered to as *secondary cells*;

- the diamond - face based - mesh, denoted by $\mathcal{D}$, whose elements will be refered to as *diamond cells*.

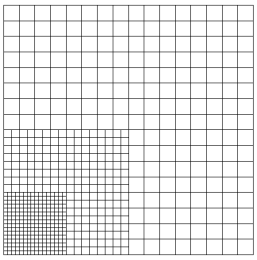

Figure 1: Mesh definition, non conformal case illustration.

**Diamond mesh $\mathcal{D}$.** Let $K \in \mathcal{M}$ and $\sigma \in \mathcal{F}_K$, the diamond cell $D_{\sigma,K}$ is the pyramid if $d = 3$ (resp. triangle if $d = 2$) with base $\sigma$ and with apex $x_K$[1]. When $\sigma \in \mathcal{F}^i$ is an interface $\sigma = K|L$, there are two diamond cells associated to $\sigma$, $D_{\sigma,K}$ and $D_{\sigma,L}$, whereas when $\sigma \in \mathcal{F}^b$, there is only one, denoted by $D_{\sigma,K}$ where $K \in \mathcal{M}$ is such that $\sigma \in \mathcal{F}_K$.

The set $\mathcal{D}$ of all the diamond cells is refered to as *the diamond mesh*.

**Secondary mesh $\mathcal{V}$.**

Definition 2.1 (Relation $\prec$) In order to define accurately subsets of $\mathcal{M}$, $\mathcal{X}$ or $\mathcal{F}$, we define the relation $\prec$ between two elements of these sets as "is a vertex of" or "is a face of". For instance, $\mathcal{F}_K$ is described by $\{\sigma \prec K\}$, and the vertices of a face $\sigma$ are $\{x_A \prec \sigma\}$.

Let $K \in \mathcal{M}$, $\sigma \in \mathcal{F}_K$. Consider the local numbering $x_1, \dots x_m$ of the $m$ ($m = 2$ in 2D, $m \in \{3, 4\}$ in 3D) vertices of $\sigma$, with the convention that $i + m = i$. In 3D, the segments $[x_{i-1}, x_i]$ and $[x_i, x_{i+1}]$ form two consecutive edges of the face $\sigma$. In this case we denote by $T_{x_i \prec \sigma \prec K}$ the union of the two tetrahedra with common base $x_i, x_\sigma, x_K$ and fourth vertex $x_{i-1}$ and $x_{i+1}$ (resp. the triangle $x_i, x_K, x_\sigma$ if $d = 2$), as depicted on figure 2.

Hence, to each node $x_A \in \mathcal{X}$ is associated a control volume denoted by $A$ and defined as

$$A = \cup_{\{x_A \prec \sigma \prec K\}} T_{x_A \prec \sigma \prec K}.$$

The *secondary mesh* $\mathcal{V}$ is the set of all these *secondary cells* $A$.

*Remark 1 (A major difference between the 2D and 3D cases)* In dimension $d = 2$ the set $\mathcal{V}$ is a non overlapping partition of $\Omega$ (see point 1. above of the definition of $\mathcal{M}$). In dimension $d = 3$ each edge $e$ of a face $\sigma$ has two endpoints along which the elements $T_{x_A \prec \sigma \prec K}$ overlap, so that the secondary control volumes overlap each others and recover exactly twice the computational domain $\Omega$: $\sum_{A \in \mathcal{V}} |A| = 2|\Omega|$.

[1] It is the convex hull of $\{\sigma, x_K\}$, if $\sigma$ is convex.

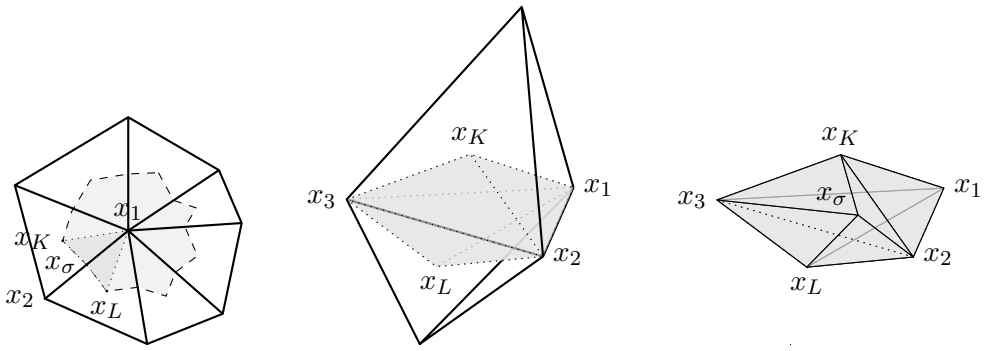


(a) Secondary cell associated to $x_1$ (dashed line) and elements $T_{x_1 \prec \sigma \prec K}$ and $T_{x_1 \prec \sigma \prec L}$ (dotted) in 2D.

(b) Cells $K$ and $L$ and diamond cells $D_{\sigma,K}$ and $D_{\sigma,L}$ (dotted) in 3D.

(c) 3D elements $T_{x_i \prec \sigma \prec K}$ and $T_{x_i \prec \sigma \prec L}$.

Figure 2: Secondary cells and Diamond cells

## 2.2 Discrete data

*Remark 2 (Measures)* The measure of any geometrical element according to its dimension (length if 1-dimensional, area or volume if 2 or 3-dimensional) is denoted by $|\cdot|$.

**Discrete tensor and boundary data.** The discrete tensor $G_h = (G_{\sigma,K})_{D_{\sigma,K} \in \mathcal{D}}$ is the data of a tensor per diamond cell, for instance the average of $G(x)$ on $D_{\sigma,K}$,

$$\forall K \in \mathcal{M}, \forall \sigma \in \mathcal{F}_K, \quad G_{\sigma,K} = \frac{1}{|D_{\sigma,K}|} \int_{D_{\sigma,K}} G(x)dx. \tag{4}$$

*Remark 3 (Meshes and discontinuities)* In the case of media heterogeneity, the tensor $G$ is discontinuous across some hypersurface $\Gamma$ inside $\Omega$. The faces of the mesh then are asked to follow that hypersurface and the discrete tensor thus reflects that heterogeneity.

Similarly the discretized boundary data are $g_h = \{(g_\sigma)_{\sigma \in \mathcal{F}_D^b}, (g_A)_{x_A \in \mathcal{X}_D^b}\}$ and $h_h = (h_\sigma)_{\sigma \in \mathcal{F}_N^b}$, for instance

$$\forall \sigma \in \mathcal{F}_D^b,\ g_\sigma = \frac{1}{|\sigma|} \int_\sigma g ds,\ \forall x_A \in \mathcal{X}_D^b,\ g_A = g(x_A), \quad \forall \sigma \in \mathcal{F}_N^b,\ h_\sigma = \frac{1}{|\sigma|} \int_\sigma h ds. \tag{5}$$

**Conservative discrete vector data.** One denotes by $\mathbf{Q}$ the set of vector valued functions $\mathbf{q} = (\mathbf{q}_{\sigma,K})_{K \in \mathcal{M}, \sigma \in \mathcal{F}_K}$ piecewise constant on the $D_{\sigma,K} \in \mathcal{D}$ (such that $\mathbf{q}_{|D_{\sigma,K}} = \mathbf{q}_{\sigma,K}$) that fulfill the *flux conservativity condition*

$$\forall \sigma = \bar{K} \cap \bar{L} \in \mathcal{F}^i, \quad G_{\sigma,K}\mathbf{q}_{\sigma,K} \cdot \mathbf{n}_\sigma = G_{\sigma,L}\mathbf{q}_{\sigma,L} \cdot \mathbf{n}_\sigma, \tag{6}$$

where $\mathbf{n}_\sigma$ is any unit normal to $\sigma$. Thus $\mathbf{q}$ can also be thought as the data of two vectors per interface $\sigma = \bar{K} \cap \bar{L} \in \mathcal{F}^i$, namely $\mathbf{q}_{\sigma,K}$ and $\mathbf{q}_{\sigma,L}$ and one vector $\mathbf{q}_{\sigma,K}$ per boundary face $\sigma \in \mathcal{F}^b \cap \mathcal{F}_K$. These values may also be denoted by $\mathbf{q}_D$ for $D \in \mathcal{D}$.

The structure inherited from $L^2(\Omega)^d$ gives the scalar product on $\mathbf{Q}$:

$$\forall \mathbf{q}^1, \mathbf{q}^2 \in \mathbf{Q}, \quad (\mathbf{q}^1, \mathbf{q}^2)_{\mathbf{Q}} = \int_\Omega \mathbf{q}^1 \cdot \mathbf{q}^2 dx = \sum_{D \in \mathcal{D}} \mathbf{q}^1_D \cdot \mathbf{q}^2_D |D|. \tag{7}$$

**Discrete scalar data.** One denotes by $\mathbb{U}$ the set of discrete scalar data defined by

$$\varphi = (\varphi^{\mathcal{M}}, \varphi^{\mathcal{V}}) = ((\varphi_K)_{K \in \mathcal{M}}, (\varphi_A)_{A \in \mathcal{V}})$$

where $\varphi_K \in \mathbb{R}$ and $\varphi_A \in \mathbb{R}$ for any $K \in \mathcal{M}$ and $A \in \mathcal{V}$. It is the data of one scalar value per primary and per secondary cell.

The space $\mathbb{U}$ is supplied with the scalar product:

$$\forall \varphi^1, \varphi^2 \in \mathbb{U}, \quad \left(\varphi^1, \varphi^2\right)_{\mathbb{U}} = \frac{1}{d} \left( \sum_{K \in \mathcal{M}} \varphi^1_K \varphi^2_K |K| + \sum_{A \in \mathcal{V}} \varphi^1_A \varphi^2_A |A| \right). \tag{8}$$

In order to take into account the Dirichlet boundary condition, we also define the affine space

$$\mathbb{U}_g = \varphi^g + \mathbb{U}_0 \subset \mathbb{U} \tag{9}$$

where $\varphi^g_K = 0$ for all $K \in \mathcal{M}$, $\varphi^g_A = g_A$ for all $x_A \in \mathcal{X}^b_D$ and $\varphi^g_A = 0$ otherwise; and

$$\mathbb{U}_0 = \{\varphi \in \mathbb{U}, \text{ such that } \forall x_A \in \mathcal{X}^b_D, \quad \varphi_A = 0\} \tag{10}$$

is a linear subspace of $\mathbb{U}$.

In dimension $d = 2$, a scalar data can be seen as the superimposition of two piecewise constant functions, one piecewise constant on the primary cells and the second one piecewise constant on the secondary cells. The coefficient $1/d$ in the previous definition thus reflects the equal importance of the two sets of cells, both recovering $\Omega$ exactly once in the measure sense.

In dimension $d = 3$ however, since the secondary cells do overlap and recover the domain exactly twice, this representation is less relevant. The coefficient $1/d$ now reflects that the secondary cells counts twice as much as the primary ones. The scalar product remains normalized: $(1, 1)_{\mathbb{U}} = |\Omega|$.

## 3 Discrete operators and discrete duality

Being given a discrete tensor $G_h$ and discrete boundary data $g_h$ and $h_h$, the principle is to define two operators, a vector flux operator $\nabla_h : \mathbb{U} \mapsto \mathbf{Q}$ and a discrete divergence $\mathrm{div}_h : \mathbf{Q} \mapsto \mathbb{U}$ that are in duality *via* a formula that mimics the Green formula in the continuous case.

### 3.1 Discrete operators

**Gradient.** Given $\varphi = (\varphi^{\mathcal{M}}, \varphi^{\mathcal{V}}) \in \mathbb{U}$, its gradient is defined in $\mathbf{Q}$ by

$$\nabla_h \varphi = (\nabla_{\sigma,K}\varphi)_{D_{\sigma,K}\in\mathcal{D}}.$$

The values $\nabla_{\sigma,K}\varphi$ per diamond cell $D_{\sigma,K}$ must fulfill the flux conservativity condition (6) and the Neumann condition (3). Therefore, some auxiliary unknowns $(\varphi_\sigma)_{\sigma\in\mathcal{F}}$ are introduced.

Any $D_{\sigma,K}$ can be split into tetrahedra (resp. triangles in dimension $d = 2$) using only the points $x_\sigma, x_K$ and $\{x_A : x_A \prec \sigma\}$, see figure 3 . Hence there is a unique function $\tilde{\varphi}$ that is piecewise affine on this tetrahedrization (resp. triangulation) and that interpolates $\varphi_K, \varphi_\sigma$ and the $(\varphi_A)_{x_A\prec\sigma}$.

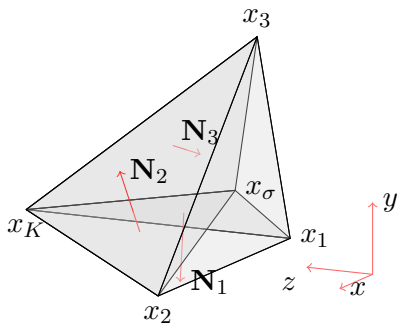


(a) 3D perspective view, triangular face

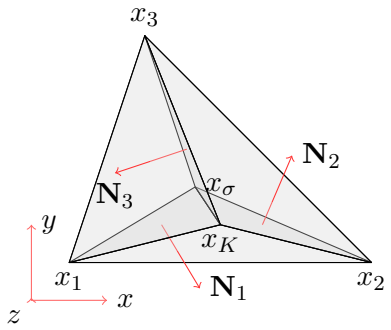


(b) Top view, triangular face

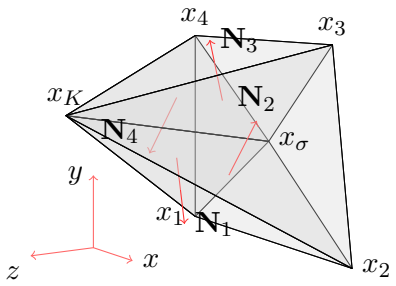


(c) 3D perspective view, quadrangular face

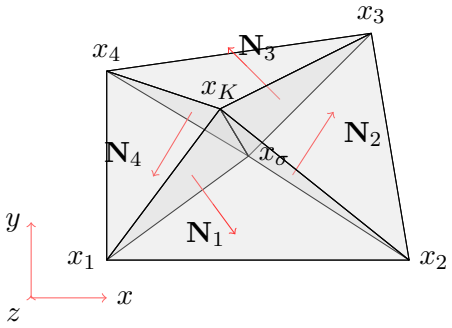


(d) Top view, quadrangular face

Figure 3: Notation inside a diamond cell $x_i \prec \sigma \prec K$ ($i = 1 \dots 3$ or 4) and orientation of the normals

For any $K \in \mathcal{M}$ and $\sigma \in \mathcal{F}_K$, the value $\nabla_{\sigma,K}\varphi$ is the vector, depending on the parameter $\varphi_\sigma$, defined by

$$\nabla_{\sigma,K}\varphi = \frac{1}{|D_{\sigma,K}|}\int_{D_{\sigma,K}} \nabla\tilde{\varphi}dx.$$

Since in each $D_{\sigma,K}$ the gradient $\nabla_{\sigma,K}\varphi$ is a linear function of $\varphi_\sigma$ (see theorem 3.1 below), the auxiliary parameters $\varphi_\sigma$ are uniquely defined and locally eliminated as follows:

- for $\sigma \in \mathcal{F}^i$ by solving eq. (6),
- for $\sigma \in \mathcal{F}_N^b$ by imposing the Neumann boundary condition

$$G_{\sigma,K}\nabla_{\sigma,K}\varphi \cdot \mathbf{n}_{\sigma K} = h_\sigma,$$

  where $\mathbf{n}_{\sigma K}$ is the unit normal to $\sigma$ outward of $K$,
- for $\sigma \in \mathcal{F}_D^b$ by imposing the Dirichlet boundary condition

$$\varphi_\sigma = g_\sigma.$$

THEOREM 3.1 (EXPRESSION OF THE GRADIENT) Consider $K \in \mathcal{M}$ and $\sigma \in \mathcal{F}_K$.

**For $\mathbf{d = 3}$**, consider the local numbering from section 2.1 (paragraph on the secondary mesh), $(x_i)_{i=1\ldots m}$ for the vertices of $\sigma$ ($m = 3$ or 4) and $(\varphi_i)_{i=1\ldots m}$ for the corresponding unknowns. Without loss of generality, one can assume that $\det(x_{i+1} - x_i, x_{i-1} - x_i, x_K - x_i) > 0$ for all $i = 1 \ldots m$ (with the convention $i + m = i$) as depicted on figure 3. Then the gradient $\nabla_{\sigma,K}\varphi$ is

$$\nabla_{\sigma,K}\varphi = \frac{1}{3|D_{\sigma,K}|}(\varphi_\sigma - \varphi_K)\mathbf{N}_{\sigma K} + \frac{1}{3|D_{\sigma,K}|}\sum_{i=1}^{m}\varphi_i(\mathbf{N}_{i-1} - \mathbf{N}_{i+1}) \tag{11}$$

with

$$\mathbf{N}_{\sigma K} = \int_\sigma \mathbf{n}_{\sigma K}\, ds = \sum_{i=1}^{m}\mathbf{N}_{\sigma,i-1,i} \quad \text{where } \mathbf{N}_{\sigma,i-1,i} = \frac{1}{2}(x_i - x_\sigma) \wedge (x_{i-1} - x_\sigma) \tag{12}$$

$$\mathbf{N}_i = \frac{1}{2}(x_K - x_\sigma) \wedge (x_i - x_\sigma), \quad i = 1 \ldots m. \tag{13}$$

**For $\mathbf{d = 2}$**, denote by $(x_i)_{i=1,2}$ the endpoints of $\sigma$ and $(\varphi_i)_{i=1,2}$ the corresponding unknowns. Without loss of generality, one can assume that $\det(x_2 - x_1, x_K - x_\sigma) > 0$. Then the gradient $\nabla_{\sigma,K}\varphi$ is

$$\nabla_{\sigma,K}\varphi = \frac{1}{2|D_{\sigma,K}|}(\varphi_\sigma - \varphi_K)\mathbf{N}_{\sigma K} + \frac{1}{2|D_{\sigma,K}|}(\varphi_2 - \varphi_1)\mathbf{N}_{12} \tag{14}$$

with

$$\mathbf{N}_{\sigma K} = -(x_2 - x_1)^\perp, \quad \mathbf{N}_{12} = (x_\sigma - x_K)^\perp,$$

and where $\cdot^\perp$ denotes the rotation of angle $+\pi/2$. By analogy with the 3D case, the normal $\mathbf{N}_{\sigma K}$ can be split:

$$\mathbf{N}_{\sigma K} = \mathbf{N}_{\sigma,1} + \mathbf{N}_{\sigma,2}, \quad \text{where } \mathbf{N}_{\sigma,1} = (x_1 - x_\sigma)^\perp,\ \mathbf{N}_{\sigma,2} = (x_\sigma - x_2)^\perp.$$

**Proof** The gradient is defined by

$$\nabla_{\sigma,K}\varphi = \frac{1}{|D_{\sigma,K}|}\int_{D_{\sigma,K}} \nabla\tilde{\varphi}dx = \frac{1}{|D_{\sigma,K}|}\int_{\partial D_{\sigma,K}} \tilde{\varphi}\mathbf{n}ds$$

where $\mathbf{n}$ is the unit normal to $\partial D_{\sigma,K}$ outside of $D_{\sigma,K}$. In 3D, $\partial D_{\sigma,K}$ is composed of the triangular facets with vertices $x_K, x_i, x_{i+1}$ and $x_\sigma, x_i, x_{i+1}$ (included in $\sigma$) on which $\tilde{\varphi}\mathbf{n}$ is an affine function. Hence we have

$$\int_{\partial D_{\sigma,K}} \tilde{\varphi}\mathbf{n}ds = \sum_{i=1}^{m} \frac{1}{3}\left(\varphi_K + \varphi_i + \varphi_{i+1}\right)\mathbf{N}_{K,i,i+1} + \sum_{i=1}^{m} \frac{1}{3}\left(\varphi_\sigma + \varphi_i + \varphi_{i+1}\right)\mathbf{N}_{\sigma,i,i+1}$$

where the vectors $\mathbf{N}_{K,i,i+1}$ and $\mathbf{N}_{\sigma,i,i+1}$ are normal to the corresponding facets, with length equal to its surface area, and outward of $D_{\sigma,K}$. This expression is reordered and then reads

$$\begin{aligned}\int_{\partial D_{\sigma,K}} \tilde{\varphi}\mathbf{n}ds = \frac{1}{3}\varphi_K \sum_{i=1}^{m} \mathbf{N}_{K,i,i+1} + \frac{1}{3}\varphi_\sigma \sum_{i=1}^{m} \mathbf{N}_{\sigma,i,i+1} \\ + \sum_{i=1}^{m} \frac{1}{3}\varphi_i \left(\mathbf{N}_{K,i,i+1} + \mathbf{N}_{K,i-1,i} + \mathbf{N}_{\sigma,i,i+1} + \mathbf{N}_{\sigma,i-1,i}\right).\end{aligned}$$

The result is derived from the observation that

$$\begin{aligned}-\sum_{i=1}^{m} \mathbf{N}_{K,i,i+1} = \sum_{i=1}^{m} \mathbf{N}_{\sigma,i,i+1} = \mathbf{N}_{\sigma K}, \\ \mathbf{N}_{K,i,i+1} + \mathbf{N}_{K,i-1,i} + \mathbf{N}_{\sigma,i,i+1} + \mathbf{N}_{\sigma,i-1,i} = \mathbf{N}_{i-1} - \mathbf{N}_{i+1},\end{aligned}$$

with the notations (12) and (13).

The 2d case is similar. ■

Definition 3.2 (Homogeneous gradient) The gradient depends linearly on $\varphi \in \mathbb{U}$ and on the discrete boundary data $g_h$ and $h_h$. The practical space for the discrete unknown is $\mathbb{U}_g = \varphi^g + \mathbb{U}_0$ (see eq. (9) and (10)). Hence the gradient is an affine function on $\mathbb{U}_g$. Its linear part is the *homogeneous gradient* $\nabla_h^0$:

$$\nabla_h^0 : \varphi \in \mathbb{U}_0 \mapsto \nabla_h\varphi - \nabla_h\varphi^g \in \mathbf{Q}. \tag{15}$$

Indeed, $\nabla_h^0\varphi$ is the gradient of $\varphi \in \mathbb{U}_0$ given by eq. (11) or eq. (14) for homogeneous boundary data $g = 0$ and $h = 0$. At last, one can write $\nabla_h\varphi = \nabla_h\varphi^g + \nabla_h^0\varphi$.

**Divergence.** Given $\mathbf{q} = (\mathbf{q}_{\sigma,K})_{K\in\mathcal{M},\sigma\in\mathcal{F}_K} \in \mathbf{Q}$, its discrete divergence is defined in $\mathbb{U}$ by $\mathrm{div}_h\,\mathbf{q} = \{(\mathrm{div}_K)_{K\in\mathcal{M}}, (\mathrm{div}_A)_{x_A\in\mathcal{X}}\}$ with

$$\forall K \in \mathcal{M}, \quad \mathrm{div}_K\,\mathbf{q} = \frac{1}{|K|}\sum_{\sigma\in\mathcal{F}_K} \mathbf{q}_{\sigma,K}\cdot\mathbf{N}_{\sigma K}, \tag{16}$$

$$\forall x_A \in \mathcal{X}, \quad \mathrm{div}_A\,\mathbf{q} = \frac{1}{|A|}\sum_{(\sigma,K):\, x_A\prec\sigma\prec K} \mathbf{q}_{\sigma,K}\cdot\mathbf{N}_{A\sigma K} \tag{17}$$

where $\mathbf{N}_{\sigma K}$ has been defined in theorem 3.1 and $\mathbf{N}_{A\sigma K}$ is the unit normal to $\partial A$ in $D_{\sigma,K}$, outward of $A$, see figure 4. This latter normal can be specified by using the local numbering $i = 1 \dots m$ and notations introduced in theorem 3.1, assuming that $x_A = x_i$:

$$\text{if } d = 3, \quad \mathbf{N}_{A\sigma K} = \begin{cases} \mathbf{N}_{i+1} - \mathbf{N}_{i-1} & \text{if } \sigma \in \mathcal{F}^i, \\ \mathbf{N}_{i+1} - \mathbf{N}_{i-1} + \mathbf{N}_{\sigma,i-1,i} + \mathbf{N}_{\sigma,i,i+1} & \text{if } \sigma \in \mathcal{F}^b \end{cases} \tag{18}$$

and

$$\text{if } d = 2, \quad \mathbf{N}_{A\sigma K} = \begin{cases} \mathbf{N}_{i\,i+1} & \text{if } \sigma \in \mathcal{F}^i, \\ \mathbf{N}_{i\,i+1} + \mathbf{N}_{\sigma,i} & \text{if } \sigma \in \mathcal{F}^b. \end{cases} \tag{19}$$

The set $\{(\sigma, K) : x_A \prec \sigma \prec K\}$ is the index set for all the diamond cells $D_{\sigma,K}$ that share $x_A$ as a common node.

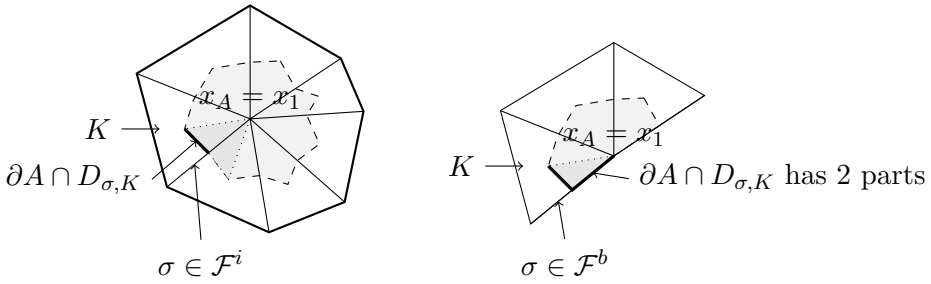


(a) Interior case, $\mathbf{N}_{A\sigma K} = \mathbf{N}_{12}$ if $x_A = x_1$.

(b) Boundary case, $\mathbf{N}_{A\sigma K} = \mathbf{N}_{12} + \mathbf{N}_{\sigma,1}$ if $x_A = x_1$.

Figure 4: The normal is $\mathbf{N}_{A\sigma K} = \int_{\partial A \cap D_{\sigma,K}} \mathbf{n}_A$ where $\mathbf{n}_A$ is the unit normal outward of the secondary control volume $A$.

*Remark 4 (Consistency and conservativity)* This definition is consistent with the Green divergence theorem by construction and because of the flux conservativity condition (6), that shows the conservativity of fluxes through the interfaces of the primary mesh $\mathcal{M}$.

**Kernel space of the Discrete gradient.** The well posedness of the scheme in section 4 depends on the injectivity properties of the homogeneous gradient $\nabla_h^0 = \nabla_h \cdot -\nabla_h \varphi^g$ (def. 3.2). Basically, if a scalar data $\varphi \in \mathbb{U}_g$ satisfies $\nabla_h \varphi = 0$ for homogeneous boundary data $g = 0$ and $h = 0$, one expects to have $\varphi = 0$.

LEMMA 3.3 Let the domain $\Omega$ be a connected set, and suppose that $\mathcal{X}_D^b \neq \emptyset$. Then the linear mapping $\nabla_h^0$ is injective in $\mathbb{U}_0$:

$$\forall \varphi \in \mathbb{U}_0, \quad \nabla_h^0 \varphi = 0 \Rightarrow \varphi = 0.$$

*Remark 5 (Pure Neumann case)* If $\mathcal{X}_D^b = \emptyset$, then $\mathbb{U}_g = \mathbb{U}$ and the conclusion is that there exists at most three constants $c_\mathcal{M}, c_\mathcal{V}^1, c_\mathcal{V}^2$ such that $\varphi_K = c_\mathcal{M}$ for all $K \in \mathcal{M}$ and $\varphi_A \in \{c_\mathcal{V}^1, c_\mathcal{V}^2\}$ for any $x_A \in \mathcal{V}$. More precisely, in the 2d case as well as in the 3d case for meshes including triangular faces, one has only two constants $c_\mathcal{M}, c_\mathcal{V}$ such that $\varphi_K = c_\mathcal{M}$ for all $K \in \mathcal{M}$ and $\varphi_A = c_\mathcal{V}$ for any $x_A \in \mathcal{V}$.

*Remark 6 (More general interfaces)* In 3D, more complex geometries for the faces lead to difficulties to describe the kernel of the discrete gradient.

**Proof** Consider $\varphi \in \mathbb{U}_0$. The gradient $\nabla_h^0 \varphi$ is given by eq. (11) or eq. (14) computed for homogeneous boundary data $g = 0$ and $h = 0$. Assume that $\nabla_h^0 \varphi = 0$ and consider a face $\sigma \in \mathcal{F}$ with vertices $(x_i)_{i=1\dots m}$ and the notations used in theorem 3.1. In the 3D case, $d = 3$, if $\sigma$ is a triangular face, $m = 3$, then the gradient rewrites

$$\nabla_{\sigma,K}\varphi = \frac{1}{3|D_{\sigma,K}|}(\varphi_\sigma - \varphi_K)\mathbf{N}_{\sigma K} + \frac{1}{3|D_{\sigma,K}|}\sum_{i=1}^{m}(\varphi_{i+1} - \varphi_{i-1})\,\mathbf{N}_i.$$

Obviously, $\mathbf{N}_1 + \mathbf{N}_2 + \mathbf{N}_3 = 0$ and then $(\mathbf{N}_1, \mathbf{N}_2, \mathbf{N}_3)$ is of rank 2 and spans the 2D plane perpendicular to $\mathbf{N}_{\sigma K}$; and consequently $\varphi_\sigma = \varphi_K$ and $\varphi_1 = \varphi_2 = \varphi_3$. If $\sigma = \bar{K} \cap \bar{L} \in \mathcal{F}^i$ then we also have $\varphi_L = \varphi_\sigma$, so that $\varphi_K = \varphi_L$.

Now, if $\sigma$ is a quadrangular face, $m = 4$, then remark that $(\mathbf{N}_1 - \mathbf{N}_3, \mathbf{N}_2 - \mathbf{N}_4)$ is of rank 2 and spans the plane perpendicular to $\mathbf{N}_{\sigma K}$. Consequently eq. (11) yields $\varphi_\sigma = \varphi_K$, $\varphi_1 = \varphi_3$ and $\varphi_2 = \varphi_4$. Similarly, if $\sigma = \bar{K} \cap \bar{L} \in \mathcal{F}^i$ we obtain $\varphi_K = \varphi_L$.

In the 2D case, $d = 2$, the face $\sigma$ has 2 endpoints $x_1, x_2$ and it is easy to see that $\varphi_\sigma = \varphi_K$ and $\varphi_1 = \varphi_2$. If $\sigma = \bar{K} \cap \bar{L} \in \mathcal{F}^i$ then $\varphi_K = \varphi_L$.

Since $\Omega$ is a connected set, it is clear from connectivity reasons that for any vertex $x_A \in \mathcal{X}$, there exists a vertex $x_B \in \mathcal{X}_D^b$ that is connected to $x_A$ trough a series of segments joining either two nodes of a triangular face or two diagonally opposite nodes in a quadrangular face, or simply the two endpoints of a face in 2D. As a consequence we have $\varphi_A = \varphi_B = 0$, since $x_B \in \mathcal{X}_D^b$ and $\varphi \in \mathbb{U}_0$.

Similarly, any cell $K \in \mathcal{M}$ is connected through a series of neighboring cells in $\mathcal{M}$ to the Dirichlet boundary, so that there exists $\sigma \in \mathcal{F}_D^b$ such that $u_K = u_\sigma = g_\sigma = 0$. ■

## 3.2 Discrete Green formula

THEOREM 3.4 (DISCRETE GREEN FORMULA) Given some discrete data $g_h, h_h$,

$$\forall \varphi \in \mathbb{U},\ \forall \mathbf{q} \in \mathbf{Q}, \quad (\mathbf{q}, \nabla_h \varphi)_\mathbf{Q} + (\mathrm{div}_h\, \mathbf{q}, \varphi)_\mathbb{U} = \langle \varphi, \mathbf{q} \cdot \mathbf{n} \rangle_{h,\partial\Omega}, \tag{20}$$

where the trace is defined by

$$\langle \varphi, \mathbf{q} \cdot \mathbf{n} \rangle_{h,\partial\Omega} = \int_{\partial\Omega} \tilde{\varphi}(\mathbf{q} \cdot \mathbf{n}) ds = \begin{cases} \sum_{\sigma \in \mathcal{F}^b} \mathbf{q}_{\sigma,K} \sum_{i=1}^{m} \frac{\varphi_\sigma + \varphi_{i-1} + \varphi_i}{3} \mathbf{N}_{\sigma,i-1,i} & \text{if } d = 3 \\ \sum_{\sigma \in \mathcal{F}^b} \mathbf{q}_{\sigma,K} \sum_{i=1}^{2} \frac{\varphi_\sigma + \varphi_i}{2} \mathbf{N}_{\sigma,i} & \text{if } d = 2 \end{cases},$$

and the function $\tilde{\varphi}$ denotes the piecewise affine interpolation of the discrete data $\varphi$ introduced in the discrete gradient definition in 3.1.

**Proof** The proof in 2D, $d = 2$, is similar to the ones found in [13] (continuous coefficients) or [3] (nonlinear fluxes).

In 3D, $d = 3$, the notation used in theorem 3.1 around a given face $\sigma \in \mathcal{F}$ (fig. 3) is still used, as well as the auxiliary variables $(\varphi_\sigma)_{\sigma\in\mathcal{F}}$ used to define the gradient $\nabla_h\varphi$ as a conservative vector data. From the definition of the inner product (8) and of the divergence (16)-(17),

$$\begin{aligned}(\mathrm{div}_h\,\mathbf{q},\varphi)_{\mathbb{U}} &= \frac{1}{3}\left(\sum_{K\in\mathcal{M}}\mathrm{div}_K\,\mathbf{q}\varphi_K|K| + \sum_{x_A\in\mathcal{X}}\mathrm{div}_A\,\mathbf{q}\varphi_A|A|\right)\\ &= \frac{1}{3}\left(\sum_{K\in\mathcal{M}}\sum_{\sigma\in\mathcal{F}_K}\mathbf{q}_{\sigma,K}\cdot\varphi_K\mathbf{N}_{\sigma K} + \sum_{A\in\mathcal{V}}\sum_{(\sigma,K):\,x_A\prec\sigma\prec K}\mathbf{q}_{\sigma,K}\cdot\varphi_A\mathbf{N}_{A\sigma K}\right).\end{aligned}$$

The first summation is reordered as follows:

$$\sum_{K\in\mathcal{M}}\sum_{\sigma\in\mathcal{F}_K}\mathbf{q}_{\sigma,K}\cdot\varphi_K\mathbf{N}_{\sigma K} = \sum_{K\in\mathcal{M}}\sum_{\sigma\in\mathcal{F}_K}\mathbf{q}_{\sigma,K}\cdot(\varphi_K-\varphi_\sigma)\mathbf{N}_{\sigma K} + \sum_{\sigma\in\mathcal{F}^b}\mathbf{q}_{\sigma,K}\cdot\varphi_\sigma\mathbf{N}_{\sigma K}$$

since $\mathbf{q}_{\sigma,K}\varphi_\sigma\mathbf{N}_{\sigma K} + \mathbf{q}_{\sigma,L}\varphi_\sigma\mathbf{N}_{L\sigma} = 0$ for $\sigma = \bar{K}\cap\bar{L}$ from the conservativity relation (6). The second summation reorders as follows, using the correspondence between the global and local numberings of vertices in the face $\sigma$ to express $\mathbf{N}_{A\sigma K}$ as in eq. (18):

$$\begin{aligned}\sum_{A\in\mathcal{V}}\sum_{(\sigma,K):\,x_A\prec\sigma\prec K}\mathbf{q}_{\sigma,K}\cdot\varphi_A\mathbf{N}_{A\sigma K} &= \sum_{K\in\mathcal{M}}\sum_{\sigma\in\mathcal{F}_K}\mathbf{q}_{\sigma,K}\cdot\sum_{i=1}^{m}\varphi_i\left(\mathbf{N}_{i+1}-\mathbf{N}_{i-1}\right)\\ &\quad+\sum_{\sigma\in\mathcal{F}^b}\mathbf{q}_{\sigma,K}\cdot\sum_{i=1}^{m}\varphi_i\left(\mathbf{N}_{\sigma,i-1,i}+\mathbf{N}_{\sigma,i,i+1}\right).\end{aligned}$$

As a consequence, we see that

$$\begin{aligned}(\mathrm{div}_h\,\mathbf{q},\varphi)_{\mathbb{U}} &= -(\mathbf{q},\nabla_h\varphi)_{\mathbf{Q}}\\ &\quad+\frac{1}{3}\sum_{\sigma\in\mathcal{F}^b}\mathbf{q}_{\sigma,K}\cdot\left(\varphi_\sigma\mathbf{N}_{\sigma K}+\sum_{i=1}^{m}\varphi_i\left(\mathbf{N}_{\sigma,i-1,i}+\mathbf{N}_{\sigma,i,i+1}\right)\right).\end{aligned}$$

But $\mathbf{N}_{\sigma K} = \sum_{i=1}^{m}\mathbf{N}_{\sigma,i-1,i}$ and then

$$\frac{1}{3}\left(\varphi_\sigma\mathbf{N}_{\sigma K}+\sum_{i=1}^{m}\varphi_i\left(\mathbf{N}_{\sigma,i-1,i}+\mathbf{N}_{\sigma,i,i+1}\right)\right) = \sum_{i=1}^{m}\frac{\varphi_\sigma+\varphi_{i-1}+\varphi_i}{3}\mathbf{N}_{\sigma,i-1,i} = \int_\sigma\tilde{\varphi}\mathbf{n}\,ds$$

where $\tilde{\varphi}$ is the piecewise linear interpolation of $\varphi$ defined in section 3.1. This concludes the proof.

■

# 4 Scheme properties and numerical analysis

## 4.1 Scheme definition

The right hand side data is defined as the vector $f_h = \{(f_K)_{K\in\mathcal{M}}, (f_A)_{A\in\mathcal{V}}\} \in \mathbb{U}$ where

$$\forall K \in \mathcal{M},\ f_K = \frac{1}{|K|}\int_K f dx, \quad \forall A \in \mathcal{V},\ f_A = \frac{1}{|A|}\int_A f dx.$$

The scheme for the numerical resolution of (1)-(3) is given as follows:

$$\text{Find } \varphi \in \mathbb{U}_g, \quad \text{such that } -\operatorname{div}_h\left(G_h \nabla_h \varphi\right) = f_h \tag{21}$$

where $G_h\mathbf{q} \in \mathbf{Q}$ is naturally defined by $(G_h\mathbf{q})_{\sigma,K} = G_{\sigma,K}\mathbf{q}_{\sigma,K}$ for all $\mathbf{q} \in \mathbf{Q}$, $K \in \mathcal{M}$ and $\sigma \in \mathcal{F}_K$.

Using the splitting $\varphi = \varphi^g + \varphi \in \varphi^g + \mathbb{U}_0$ from eq. (9) and definition 3.2 of the homogeneous gradient, problem (21) is obviously equivalent to the linear system

$$-\operatorname{div}_h(G_h\nabla_h^0\varphi) = f_h + \operatorname{div}_h(G_h\nabla_h\varphi^g) \tag{22}$$

for the unknown $\varphi$ in $\mathbb{U}_0$.

THEOREM 4.1 (WELL-POSEDNESS OF THE DISCRETE PROBLEM) If $\mathcal{F}_D^b \neq \emptyset$ then eq. (22) is a symmetric and positive definite system of linear equations, so that eq. (21) has a unique solution $\varphi \in \mathbb{U}_g$.

*Remark 7 (Pure Neumann case)* When $\mathcal{F}_D^b = \emptyset$, the problem can also be solved, but leading to the same difficulties as in the continuous case. The linear system remains symmetric positive. It is however no longer definite: its kernel corresponding to the discrete gradient operator kernel specified in remark 5. As a result, eventual solutions are given up to additive constants. The existence of solutions in that case requires a compatibility condition equivalent with the following one in the continuous case: $\int_\Omega f dx + \int_{\partial\Omega} h ds = 0$.

**Proof** We recall that the operator $\nabla_h^0$ used in the equivalent formulation (22) is the gradient operator for homogeneous boundary data $g = 0$ and $h = 0$ and $\varphi \in \mathbb{U}_0$ is the linear part in $\varphi = \varphi^g + \varphi$. The discrete duality relation (20) proves that

$$\forall \psi \in \mathbb{U}_0, \quad \left(-\operatorname{div}_h\left(G_h\nabla_h^0\varphi\right), \psi\right)_{\mathbb{U}} = \left(G_h\nabla_h^0\varphi, \nabla_h\psi\right)_{\mathbf{Q}},$$

so that the system is symmetric and

$$\left(-\operatorname{div}_h\left(G_h\nabla_h^0\varphi\right), \varphi\right)_{\mathbb{U}} = \left(G_h\nabla_h^0\varphi, \nabla_h^0\varphi\right)_{\mathbf{Q}} \geq 0,$$

so that it is positive. From lemma 3.3 we derive that

$$\left(G_h\nabla_h^0\varphi, \nabla_h^0\varphi\right)_{\mathbf{Q}} = 0 \Rightarrow \varphi = 0,$$

if $\mathcal{X}_D^b \neq \emptyset$ and then the linear system (22) is symmetric and positive definite. Hence, it has a unique solution $\varphi \in \mathbb{U}_0$ and then there exists a unique solution to eq. (21), namely $\varphi = \varphi^g + \varphi$. ■

### 4.2 Numerical analysis of the method

The convergence of the method is investigated on a simple test case. Comparisons with the classical $P^1$ finite element (FE) method are provided both in terms of accuracy and of computational costs.

The test case considered here consists in solving eq. (1)-(3) with $G(x) = \mathrm{Id}$ and homogeneous Dirichlet boundary conditions, $g = 0$ and $\partial\Omega_D = \partial\Omega$ on the domain $\Omega = (0,1)^d$. We choose the exact solution to be

$$\forall x = (x_1, \dots x_d), \quad \varphi(x) = \sin(2\pi x_1) \dots \sin(2\pi x_d),$$

so that the right hand side of (1) is $f(x) = -\,d\,4\pi^2 \sin(2\pi x_1) \dots \sin(2\pi x_d)$.

Given a conformal triangulation or tetrahedrization $\mathcal{M}_h$ of size $h$, two approximate solutions are computed, the DDFV solution $\varphi_h^{DDFV}$ and the $P^1$ FE solution $\varphi_h^{FE}$. Both systems being symmetric positive definite, the same method (a preconditioned conjugate gradient) has been used for the system inversion, using the same preconditioning technique (SSOR). Thus, the computational cost of both methods can be easily compared. The accuracy for the DDFV and FE methods in the $L^2(\Omega)$ norm are respectively defined as

$$\left(e_h^{DDFV}\right)^2 = \frac{\int_\Omega |\tilde{\varphi}_h^{DDFV} - \varphi|^2 dx}{\int_\Omega |\varphi|^2 dx}, \quad \left(e_h^{FE}\right)^2 = \frac{\int_\Omega |\varphi_h^{FE} - \varphi|^2 dx}{\int_\Omega |\varphi|^2 dx}. \tag{23}$$

where $\tilde{\varphi}_h^{DDFV}$ is the piecewise affine and continuous ($P^1$) reconstruction used in section 3.1. The $H_0^1$ semi-norm error is defined as

$$\left(e_h^{DDFV,1}\right)^2 = \frac{\int_\Omega |\nabla_h \varphi_h^{DDFV} - \nabla\varphi|^2 dx}{\int_\Omega |\nabla\varphi|^2 dx}, \quad \left(e_h^{FE,1}\right)^2 = \frac{\int_\Omega |\nabla\varphi_h^{FE} - \nabla\varphi|^2 dx}{\int_\Omega |\nabla\varphi|^2 dx}. \tag{24}$$

**2D case** The DDFV scheme and the $P^1$ FE methods are compared on a series of 7 successively refined triangular meshes. The results are displayed on figure 5.

Both methods exhibit the same expected order 2 of convergence in $L^2$ norm with respect to the mesh size. On a given mesh, the DDFV scheme appears to be more accurate: it is actually as accurate as the $\mathrm{P}^1$ method on the following refined mesh counting four times more vertices. That comparison is however unfair since on this given mesh the methods have different numbers of degrees of freedom (DOF): in dimension 2 the DDFV scheme has three times more DOF as the $\mathrm{P}^1$ method. Thus, since an order of refinement multiplies the number of DOF by 4, the DDFV scheme appears to be more accurate than the $\mathrm{P}^1$ method when compared at equal number of DOF, with a factor 4/3. Again, that comparison is not entirely fair, since at equal number of DOF, the systems fill-in patterns are different leading to different computational costs during the inversion. We therefore compared the computational costs for both methods for a given accuracy in $L^2$ norm, which comparison can be performed since the systems are inverted with the same iterative solver and preconditioner. The two methods display the same complexity, the DDFV method cost being smaller with a benefit of 25%.

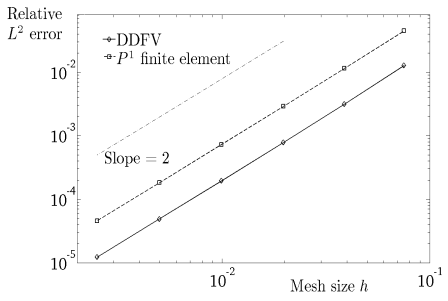


(a) Accuracy in the $L^2$ norm with respect to the mesh size. The expected order 2 for both methods is observed.

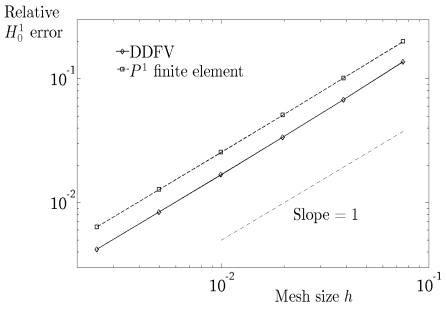


(b) Accuracy in the $H_0^1$ semi-norm with respect to the mesh size. The expected order 1 for both methods is observed.

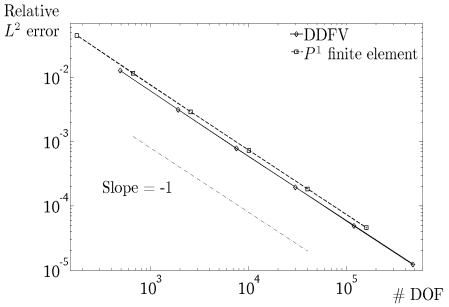


(c) Accuracy in the $L^2$ norm with respect to the number of DOFs.

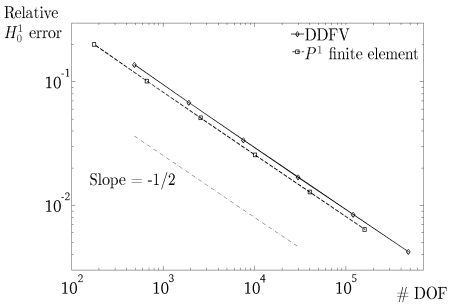


(d) Accuracy in the $H_0^1$ semi-norm with respect to the number of DOFs.

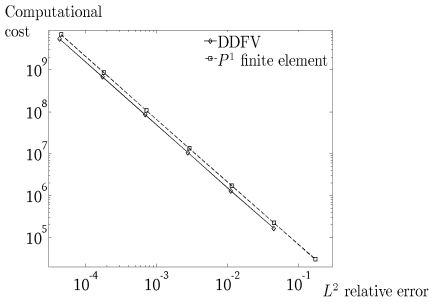


(e) Computational cost with respect to accuracy in the $L^2$ norm. The same complexity is observed.

Figure 5: 2D case. Numerical comparison between the DDFV scheme and the $P^1$ finite element method.

**3D case** The DDFV scheme and the $P^1$ FE method are here compared on a series of 4 successively refined tetrahedral meshes. The number of mesh vertices roughly

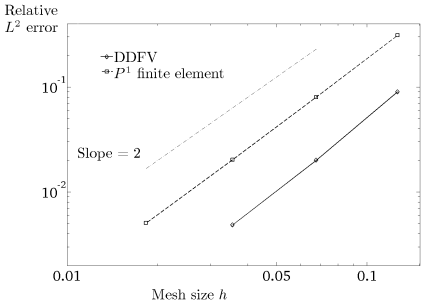


(a) Accuracy in the $L^2$ norm with respect to the mesh size. The expected order 2 for both methods is observed.

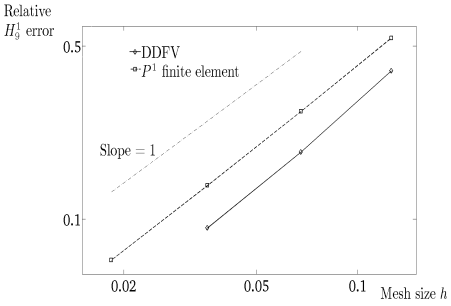


(b) Accuracy in the $H_0^1$ semi-norm with respect to the mesh size. The expected order 1 for both methods is observed.

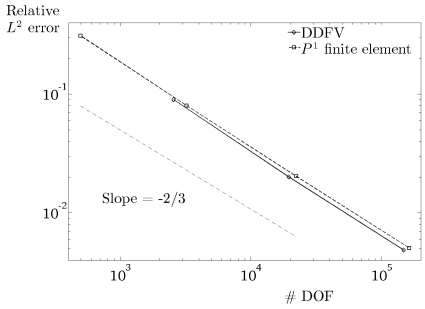


(c) Accuracy in the $L^2$ norm with respect to the number of DOFs.

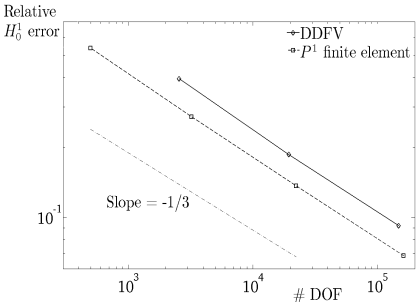


(d) Accuracy in the $H_0^1$ semi-norm with respect to the number of DOFs.

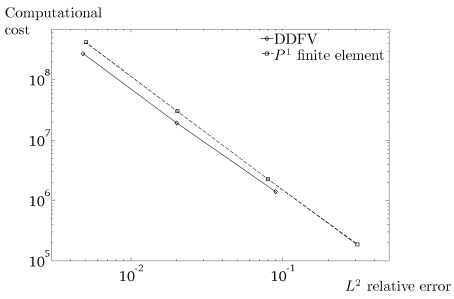


(e) Computational cost with respect to accuracy in the $L^2$ norm. The same complexity is observed.

Figure 6: 3D case. As above, this figure displays the numerical comparison between the DDFV scheme and the $P^1$ FE method.

varies from 500 to 200 000. The results are displayed on figure 6.

The DDFV scheme, as compared with the $P^1$ FE scheme, displays the same

behavior as in the two dimensional case. On a given mesh, the DDFV scheme is much more accurate, actually as accurate as the $P^1$ on the following refined mesh, counting roughly 7.5 times more vertices. Since on a given mesh in 3D, the DDFV scheme uses 6 times more DOF, the DDFV scheme remains more accurate at equal number of DOF. Eventually, when comparing the computational costs for a prescribed accuracy, the DDFV scheme appears slightly more efficient than the $P^1$ FE method.

# 5 Application to the heart electrical activity simulation

## 5.1 Medical data processing: From medical images to meshes

We now explain how we construct an accurate 2D mesh of the heart and torso that will be suitable for applying the DDFV method to simulations of the heart electrical activity. This is done in two steps. First we segment the heart and torso from a medical image, then we generate a mesh based on this segmentation. This is done using a high resolution computed tomography (CT) scan, courtesy of the Ottawa Heart Institute. Each 2D slice of the CT is of size $512 \times 512 \times 199$ and the resolution is 0.49 mm $\times$ 0.49mm $\times$ 1.25mm. To construct the 2D model of the torso, an horizontal slice has been extracted from the data set.

The medical image can be thought as a function $g : \Omega \to \mathbb{R}$. The segmentation is then performed using the Chan-Vese model [5], which seeks for the best approximation of the image $g$ by a binary image $u$, in the sense that $u$ minimizes the constrained Mumford-Shah problem:

$$\min_{u \in X} |J_u| + \int_\Omega |g - u|^2 dx,$$

where $X$ denotes the set of binary functions in $SBV(\Omega)$ and $|J_u|$ is the (1-dimensional) Haussdorf measure of the jump set of $u$. For a detailed presentation of Mumford-Shah functional as well as for $BV$ and $SBV$ spaces, the reader is refered to [1].

The problem can be reformulated using level sets, in order to be able to do a gradient descent, which will be solved by explicit finite difference scheme on the underlying image grid.

This process splits the image into two main components. Applying this iteratively will allow to decompose the medical image as a piecewise constant image, from which the region of interest can be extracted. This new iterative Chan-Vese technique has been presented in [24, 22]. Figure 7 shows the results of this iterative segmentation process on the 2D image of the heart. The boundary of the heart is described implicitly via a level set function, that is, a function whose zero level curve is the boundary of the heart. The mesh generation is made using DistMesh [20], a simple and powerful mesher for domains implicitly defined through a level set function. DistMesh has a new approach of mesh generation for domains implicitly defined. It has been modified to suit our needs (subdomains). Figure 8 shows the mesh generated from the segmentation together with the given subdomains: lungs, ventricles, ventricles cavities and remaining tissues.

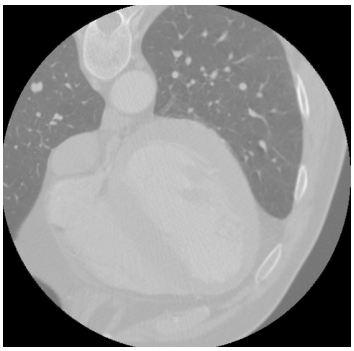

(a) 2D medical image extracted from a 3D CT Scan (courtesy of the Ottawa Heart Institute).

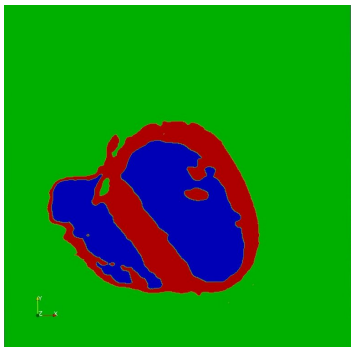

(b) The corresponding segmented image.

Figure 7: Iterative and automatic image segmentation.

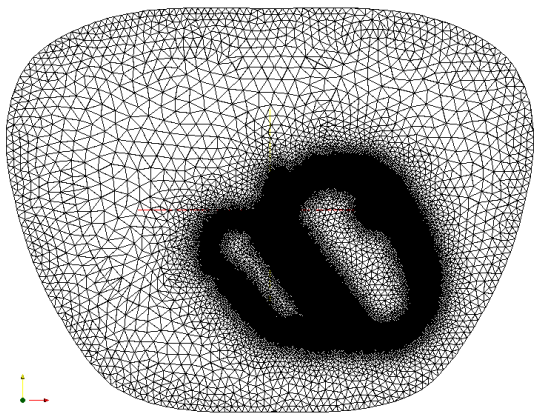

(a) Mesh of the whole torso.

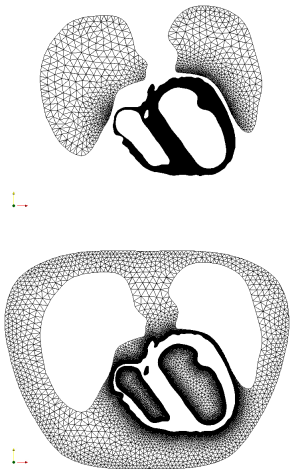

(b) Meshes of the lungs and ventricles (top) and meshes of the cavities and remaining torso (bottom).

Figure 8: Meshes of a 2D thorax slice. 600 000 vertices in total, 500 000 in the ventricles

## 5.2 The model

The modified monodomain model (see [6, 7]) describes the electrical activity of the heart inside the torso. It involves two compartments inside the myocardium: the intra- and extracellular media. The extracellular potential $\varphi$ further extends inside

the cavities and outside to the whole torso. This extended potential is supposed to be at electrostatic equilibrium. Electrocardiograms (ECG) are measures of $\varphi$ at given points of the surface of the torso. Aside from $\varphi$, the modified monodomain model also describes the evolution of the transmembrane potential which is the difference between the intra- and extracellular potentials: $v = \varphi_i - \varphi$. This transmembrane potential $v(x,t)$ is given directly as the solution of a reaction-diffusion system involving a second variable $\mathbf{w}(x,t) \in \mathbb{R}^m$ that describes the cells membrane activity using a set of ODEs. Depending on the level of realism, several ionic models exist where $m$ is up to 20. It is important to note that some of the most important ODEs of these ionic models are stiff. The resulting ionic current $I_{ion}(v,\mathbf{w})$ is used to simulate the normal propagation of depolarization and repolarization wave fronts ($v$ passing from a rest value to a plateau value and back to its rest value). It reads in $H$,

$$A_0\left(C_0\frac{\partial v}{\partial t} + I_{ion}(v,\mathbf{w})\right) = \operatorname{div}(G_1\nabla v) + I_{app}(x,t), \quad \frac{\partial \mathbf{w}}{\partial t} = g(v,\mathbf{w}), \tag{25}$$

while the electrostatic balance equation on $\Omega = H \cup T$ is

$$-\operatorname{div}(G\nabla\varphi(t)) = [\operatorname{div}(G_3\nabla v(t))]\,1_H \tag{26}$$

The data $A_0$ and $C_0$ are constant scalars, the tensor $G_1 = G_1(x)$ is non constant and anisotropic, $I_{ion}$, $g$ are reaction terms, $I_{app}$ is an externally applied current that activates the system and in equation (26), $G = G(x)$ and $G_3 = G_3(x) = G_1(x) + G_2(x)$ are non constant tensors.

The local orientation of the muscle fibers inside the myocardium is represented in the anisotropic diffusion tensors, $G_1(x)$ (in eq. (25)) and $G_2(x)$, $G_3(x)$ (in eq. (26)). They all have the form $G_i(x) = P^{-1}(x)D_iP(x)$ $(i = 1,2,3)$ where $D_i$ is diagonal, representing longitudinal and transverse conductivities, and $P(x)$ is a change of basis matrix from the Frenet basis attached to the fiber's direction at point $x$.

At last, the global conductivity matrix $G = G(x)$ is used to take into account the difference of conductivity between the lungs, ventricular cavities, etc.

$$G(x) = \begin{cases} G_2(x) & \text{for } x \in H, \\ G_{\text{cavities}} & \text{in the ventricular cavities,} \\ G_{\text{lung}} & \text{inside the lungs,} \\ G_0 & \text{otherwise.} \end{cases} \tag{27}$$

A homogeneous Neumann condition is set on the boundary $\partial\Omega$ to express from eq. (26) that no current flows out of the torso.

Equation (25) is decoupled from (26). Its solution is computed first, using DDFV discretisation together with a semi implicit time-integration: implicit for the diffusion and explicit for the reaction. The constraints on the time step both rely on the reaction stiffness (the ionic dynamic at the cellular scale) and on the consistency with the space resolution of the mesh. Numerical experiment not shown here indicate that a 1/20 milli-second (ms) time step is sufficient to get accurate solutions for the case presented here. Once equation (25) has been solved on the whole time interval, equation (26) is solved using the precomputed values of $v(\cdot,t_n)$ at times $t_n$ as

right hand side, so reconstructing the potential field $\varphi(\cdot, t_n)$ on the whole domain at the same instant. Equation (26) being a space problem only, no time step constraint holds here: the frequency it has to be solved thus is arbitrary. This frequency has been set here in order to recover an ECG of good quality, namely at each ms.

Problem (26) exactly is of the form (1)-(3) with a discontinuous and anisotropic diffusion tensor $G(x)$ given in (27). It has been discretised using the DDFV method, the Neumann boundary condition is taken into account imposing a zero mean value condition on the solution. Its numerical resolution is highly demanding because of the mesh size (see the next paragraph for the details) together with the ill-conditioning of discretised elliptic problems. In practice, thanks to the symmetry of the discrete matrix, a CG solver is used here with SSOR preconditioning.

### 5.3 Simulation

As an illustration, the following simulation of a whole cardiac cycle is performed. The geometry and mesh are extracted from segmented data and are shown on figure 8. The mesh consists in roughly 600 000 degrees of freedom (485 000 in $H$), such a fine mesh being required inside the heart to account for the dynamics of the reaction-diffusion system (25).

The values of conductivities are taken from [19]. They are summarized in the following table:

| Tensor | fibers' direction | orthogonal directions |
|---|---|---|
| $G_1$ | 1.740 | 0.1934 |
| $G_2$ | 3.906 | 1.970 |
| $G_0$ | 2.200 | 2.200 |
| $G_{lung}$ | 0.500 | 0.500 |
| $G_{cavities}$ | 6.700 | 6.700 |

Inside the heart, these anisotropic tensors are considered. Aside from the heart, conductivities are isotropic but heterogeneous from one organ to another.

The ionic current $I_{ion}$ is computed using the model of Ten Tussher & al [23]. This model of human ventricular cell uses 15 ODEs and several other variables thus $m$, the size of $w$, is greater than 20. The externally applied current $I_{app}$ consists of a 2 $ms$ impulsion starting at time $t = 20$ $ms$. It is located on several zones of the myocardium according to experiment [14].

A complete cardiac cycle of 600 ms has been simulated. As stated above, the extended potential $\varphi$ is computed at each ms: so meaning 600 inversion on the whole cycle. The values of $\varphi$ are recorded at 6 points on the body surface so providing the ECG depicted in figure 10 (b). The whole extracellular and extracardiac electrical field in shown on figure 10 (a), left. The action potential wavefront and its isochrones are shown on figure 9.

## References

[1] L. Ambrosio, N. Fusco, and D. Pallara. Functions of bounded variation and free discontinuity problems. *Oxford Mathematical Monographs*, 2000.

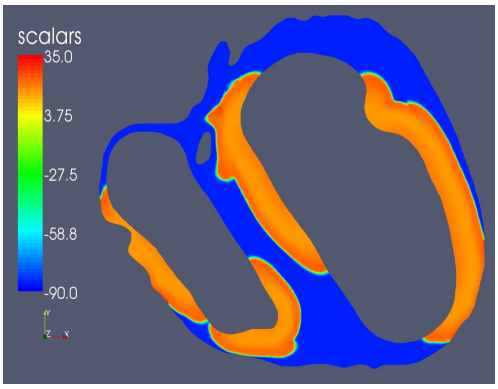


(a) Excitation potential wave $V_m$ 30 ms after initiation.

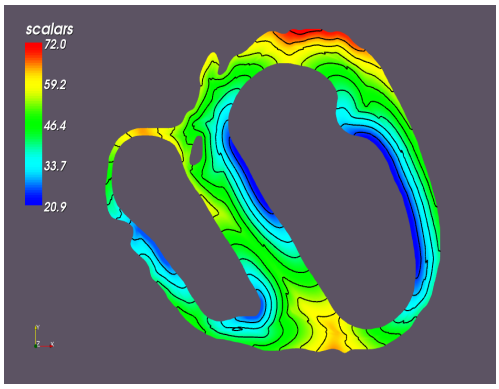


(b) Corresponding isochrones of the excitation process, 5 ms separates every isoline.

Figure 9: Heart excitation pattern.

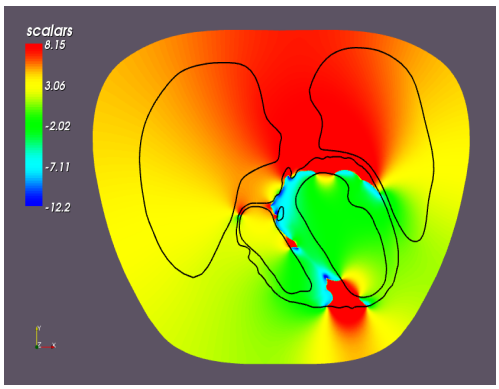


(a) Torso and cardiac extracellular potential field 30 ms after initiation (synchronous with the graphics in figure 9), observe that the changes in $\varphi$ correspond to the breakthrough of the excitation wave on the epicardiac surface.

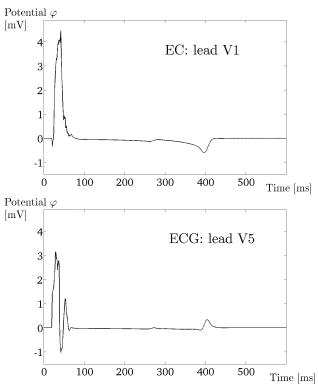


(b) Recorded body surface potential at 2 different torso locations (V1 and V5 leads, x-axis in ms and y-axis in mV).

Figure 10: Torso potential pattern.

[2] B. Andreianov and M. Bendahmane. On Discrete Duality Finite Volume discretization of gradient and divergence operators in 3D. http://hal.archives-ouvertes.fr/hal-00355212/en/.

[3] B. Andreianov, F. Boyer, and F. Hubert. Discrete duality finite volume schemes for Leray-Lions-type elliptic problems on general 2d meshes. *Num. Meth. for PDEs*, 23(1):145–195, 2007. http://dx.doi.org/10.1002/num.20170.

[4] F. Brezzi, K. Lipnikov, and M. Shashkov. Convergence of the mimetic finite dif-

ference method for diffusion problems on polyhedral meshes. *SIAM J. Numer. Anal.*, 43(5):1872–1896, 2005.

[5] T.F. Chan and L.A. Vese. Active contours without edges. *Image Processing, IEEE Transactions on*, 10(2):266–277, 2001.

[6] J.C. Clements, J. Nenonen, and M. Horacek. Activation Dynamics in Anisotropic Cardiac Tissue via Decoupling. *Annals of Biomed. Eng.*, 32(7):984–990, 2004.

[7] P. Colli-Franzone, LF. Pavarino, and B. Taccardi. Simulating patterns of excitation, repolarization and action potential duration with cardiac Bidomain and Monodomain models. *Math. Biosci.*, 197(1):35–66, 2005.

[8] Y. Coudière, T. Gallouët, and R. Herbin. Discrete sobolev inequalities and $L^p$ error estimates for finite volume solutions of convection diffusion equations. *Math. Model. Numer. Anal.*, 35(4):767–778, 2001.

[9] Y. Coudière and F. Hubert. A 3d discrete duality finite volume method for nonlinear elliptic equations. In *Algoritmy, Conference on Scientific Computing*, Slovakia, 2009.

[10] Y. Coudière and C. Pierre. Stability and convergence of a finite volume method for two systems of reaction-diffusion equations in electro-cardiology. *Nonlinear Anal. Real World Appl.*, 7(4):916–935, 2006.

[11] Y. Coudière, J. P. Vila, and P. Villedieu. Convergence rate of a finite volume scheme for a two dimensionnal diffusion convection problem. *Math. Model. Numer. Anal.*, 33(3):493–516, 1999.

[12] S. Delcourte, K. Domelevo, and P. Omnes. A discrete duality finite volume approach to Hodge decomposition and div-curl problems on almost arbitrary two-dimensional meshes. *SIAM J. Numer. Anal.*, 45(3):1142–1174, 2007.

[13] K. Domelevo and P. Omnes. A finite volume method for the laplace equation on almost arbitrary two-dimensional grids. *M2AN*, 39(6):1203–1249, 2005.

[14] D. Durrer, RT. Van Dam, GE. Freud, Janse MJ., Meijler FL., and ArzBaecher RC. Total excitation of the isolated human heart. *Circulation*, 41:899–912, 1970.

[15] R. Eymard, T. Gallouët, and R. Herbin. *Handbook of Numerical Analysis*, chapter Finite Volume Methods. Elsevier, North-Holland, 2000.

[16] R. Herbin and F. Hubert. Benchmark on discretization schemes for anisotropic diffusion problems on general grids. In *Finite Volume For Complex Applications, Problems And Perspectives. 5th International Conference*, pages 659–692. London (UK), Wiley, 2008.

[17] F. Hermeline. A finite volume method for the approximation of diffusion operators on distorted meshes. *Journal of Computational Physics*, 160(2):481–499, 2000.

[18] F. Hermeline. Approximation of 2-d and 3-d diffusion operators with variable full tensor coefficients on arbitrary meshes. *Computer Methods in Applied Mechanics and Engineering*, 196(21):2497–2526, 2007.

[19] P. Le Guyader, F. Trelles, and P. Savard. Extracellular measurement of anisotropic bidomain myocardial conductivities. I. theoretical analysis. *Annals Biomed. Eng.*, 29(10):862–877, 2001.

[20] P.O. Persson and G. Strang. A Simple Mesh Generator in MATLAB. *SIAM Review*, 46(2):329–345, 2004.

[21] C. Pierre. *Modélisation et simulation de l'activité électrique du coeur dans le thorax, analyse numérique et méthodes de volumes finis*. PhD thesis, Université de Nantes, 2005.

[22] O. Rousseau and Y. Bourgault. An iterative active contour algorithm applied to heart segmentation. SIAM Conference on Imaging Science. San Diego, CA, 7-9 July, 2008.

[23] K.H. Ten Tusscher, D. Noble, P.J. Noble, and A.V. Panfilov. A model for human ventricular tissue. *Am. J. Physiol. Heart. Circ. Physiol.*, 286(4), 2004.

[24] A. Tsai, A. Yezzi Jr, and A.S. Willsky. Curve evolution implementation of the Mumford-Shah functional for image segmentation, denoising, interpolation and magnification. *IEEE Trans. Image Processing*, 10(8):1169–1186, 2001.